

PHOTONICS Research

Improving long-term temperature bias stability of an integrated optical gyroscope employing a Si_3N_4 resonator

CHANGKUN FENG,¹ YONGGUI ZHANG,¹ HONGHAO MA,¹ HUI LI,^{1,2} AND LISHUANG FENG^{1,3}

¹School of Instrumentation and Optoelectronics Engineering, Beihang University, Beijing 100191, China

²e-mail: lihui@buaa.edu.cn

³e-mail: fenglishuang_cn@hotmail.com

Received 14 February 2022; revised 19 May 2022; accepted 22 May 2022; posted 23 May 2022 (Doc. ID 456321); published 30 June 2022

The presence of polarization noise generated by the waveguide resonator limits the performance of a resonant integrated optical gyroscope (RIOG). Using silicon nitride (Si_3N_4) to fabricate a waveguide with an ultralow-aspect-ratio can result in a resonator that only supports light transmission in a single-polarization state, suppressing polarization noise. We successfully fabricated a Si_3N_4 resonator with a bending radius of 17.5 mm, a finesse (F) of 150, a quality factor (Q) of 1.54×10^7 , and a propagation loss of 1.2 dB/m. The Si_3N_4 resonator was used to construct a double closed-loop RIOG that showed long-term bias stability (3600 s) of 13.2°/h at room temperature, 14.8°/h at 40°C, 21.2°/h at 50°C, and 23.6°/h at 60°C. We believe this to be the best performance reported to date for a Si_3N_4 resonator-based RIOG. This advancement paves the way for the wider application of RIOGs. © 2022 Chinese Laser Press

<https://doi.org/10.1364/PRJ.456321>

1. INTRODUCTION

With the development of integrated photonics, high-performance waveguide resonators have found wide applications, such as in ultranarrow linewidth lasers [1–3], optical frequency combs [4–6], optical gyroscopes [7], and biosensors [8,9], and are playing an increasingly important role. At the same time, resonant integrated optical gyroscopes (RIOGs) based on waveguide resonators are becoming more accurate, smaller in size, and more highly integrated [10,11]. At present, low-cost micro-electro-mechanical system (MEMS) gyroscopes are commonly used in the market, and the long-term bias stability is greater than about 10°/h, which belongs to the category of medium and low precision. However, compared with RIOG, MEMS-based gyroscopes are less resistant to shock and vibration, further limiting their applications. The RIOGs employ monolithic integration or hybrid integration technology to integrate part, or all, of the light source, modulator, beam splitter, detector, and other devices on a chip to realize micro-systemization. RIOGs measure rotational angular velocity by detecting the resonant frequency difference caused by the Sagnac effect [12]. Its core component is the waveguide resonator, and the design and manufacture of high-performance integrated optical resonators is the key to improving the performance of the RIOG.

The sensitivity of the RIOG is a function of the quality factor (Q) and finesse (F) of the waveguide resonator [13]. To obtain a higher performance resonator, it is necessary to

reduce the loss as much as possible. The scattering will cause backscattered noise, distorting even the resonance curve [14,15], which affects the ultimate sensitivity of the gyroscope. By using different frequency modulation and carrier suppression methods for clockwise (CW) light waves and counter-clockwise (CCW) light waves, backscattered noise can be effectively reduced [16,17]. Advanced processing techniques are used to improve the purity of the waveguide material and the smoothness of the surface to reduce backscattered noise. Meanwhile, due to the birefringence effect of the optical waveguide, the waveguide resonator can excite two orthogonal intrinsic polarization states (i.e., primary polarization state and secondary polarization state). The secondary polarization state will exist as noise and affect the long-term bias stability of the gyroscope. Unlike with backscattered noise, there has to date been no substantial progress on reducing the polarization fluctuation noise that affects the long-term stability of the RIOG. The most effective method of doing so would be to make a resonator that only supports light propagation in a single-polarization state [18,19].

Many materials can be used to make a resonator, such as polymers [20,21], silica [22], and Si_3N_4 waveguide [23,24]. The polarization extinction ratio (PER) of the waveguide resonator made of polymer materials can reach 39 dB [21], but the propagation loss is high. For silica waveguides, the propagation loss can be as low as 0.1 dB/m [22]. Because of this advantage, most of the reported RIOGs are based on silica

resonator. For example, Ma *et al.* proposed a high-accuracy feedback loop with low-delay for a high-performance gyroscope, improving the dynamic range [25]. Reference [26] reported that the long-term bias stability of the gyroscope reached 10°/h by improving the system reciprocity. However, the symmetrical structure makes the PER of the silica waveguide resonator relatively low. So, there are few reported results of temperature-related tests on RIOGs based on silica resonators. In recent years, Si₃N₄ waveguides that can achieve ultra-high Q have received more and more attention. Due to the recent progress in Si₃N₄, it has been used in numerous fields [27], including light detection and ranging [28], on-chip delay lines [29], and so on.

At present, many research institutions have conducted a lot of research on Si₃N₄ waveguides and prepared Si₃N₄ microcavities of various sizes according to different needs. Lipson *et al.* produced a Si₃N₄ microcavity with a bending radius of 115 μm and a measured propagation loss of 0.8 dB/m at 1560 nm [30]. Kippenberg *et al.* achieved a propagation loss of 5 dB/m at 1550 nm in a Si₃N₄ microcavity with a bending radius of 230 μm [31]. Paul *et al.* designed and fabricated a Si₃N₄ microcavity with a bending radius of 300 μm and propagation loss of 0.46 dB/cm at 780 nm [32]. Poon *et al.* produced a Si₃N₄ microcavity with a bending radius of 115 μm and propagation loss of about 0.15 dB/cm at 1550 nm [33].

The Si₃N₄ microcavities above were mostly designed to be high-constrained waveguides used in narrow linewidth lasers or optical frequency combs. There are few reports on the Si₃N₄ resonator designed for the RIOG. To achieve the single-polarization performance of resonator, the Si₃N₄ waveguide adopts an ultralow-aspect-ratio structure, and shape birefringence causes polarization-dependent loss. By using an ultralow-aspect-ratio core geometry, a total propagation loss of (0.045 ± 0.04) dB/m for a 40 nm \times 13 μm Si₃N₄ waveguide has been reported [34]. Bowers *et al.* designed a Si₃N₄ resonator with a bending radius of 9.65 mm and a propagation loss of 0.3 dB/m at 1580 nm [35]. Meanwhile, according to the latest progress, Blumenthal *et al.* produced a Si₃N₄ resonator with a bending radius of 11.787 mm and a propagation loss of about 0.7 dB/m [36]. But they did not employ it into the RIOG system for testing. In our previous work, we successfully fabricated Si₃N₄ resonators with bending radius of 17.5 mm and 8 mm, and the propagation losses were 2.5 dB/m and 2.46 dB/m, respectively [18,19]. Meanwhile, a gyroscope test system incorporating the Si₃N₄ resonator with a bending radius of 8 mm was built. However, due to high propagation loss, the long-term bias stability was only 0.68°/s [18]. As high propagation loss limits the performance of the RIOG, designing a low-loss processing technology is crucial for realizing high-performance Si₃N₄ resonators.

In this paper, a transmissive Si₃N₄ bus coupled resonator with a bending radius of 17.5 mm is successfully fabricated, with a 40 nm thick and 4 μm wide design. The resonator has a measured F of 150, a Q of 1.54×10^7 , and a propagation loss of 1.2 dB/m. In tests, it showed excellent single-polarization performance in a range of temperatures. An RIOG test system incorporating the Si₃N₄ resonator was built that showed long-term bias stability of 13.2°/h at room temperature, 14.8°/h at

40°C, 21.2°/h at 50°C, and 23.6°/h at 60°C. The test results had higher repeatability and stability than RIOG based on a silica waveguide resonator. We believe this to be the best performance reported to date for the Si₃N₄ resonator-based RIOG.

2. THEORETICAL SIMULATION

The sensitivity of an RIOG can be defined as [37]

$$\delta\Omega = \frac{\lambda c}{6FAN} \sqrt{\frac{e}{tI_{\text{PD_max}}}}, \quad (1)$$

$$F = \frac{\pi}{\arccos[2q/(1+q^2)]}, \quad (2)$$

where λ is the wavelength of light ($\lambda = 1550$ nm), c is the speed of light ($c = 3 \times 10^8$ m/s), F is the finesse, A is the effective area ($A = \pi R^2$, $R = 17.5$ mm), N is the number of the waveguide resonator loops, e is the electron charge ($e = 1.6 \times 10^{-19}$ C), t is the integration time ($t = 10$ s), and $I_{\text{PD_max}}$ is the maximum photocurrent generated by the photodetector without saturation ($I_{\text{PD_max}} = 1$ mA). $q = (1 - k_c)(1 - a_c)(1 - a_{L/2})$, k_c is the coupling coefficient, a_c is the additional amplitude loss of the coupler, and $a_{L/2}$ is the half-turn propagation amplitude loss of waveguide resonator. Also, the additional loss of the coupler will increase with the increase of the coupling coefficient. Therefore, the additional loss is not a fixed value. In the simulation, it is assumed that $a_c = 0.1k_c$. We can see from Eqs. (1) and (2) that the propagation loss α_L of the resonator has a great influence on the sensitivity when the diameter of the resonator is constant.

Figure 1 shows the relationship between the sensitivity and coupling coefficient for gyroscopes under different waveguide propagation loss conditions when the resonator diameter is 35 mm. When the propagation loss is lower, the sensitivity of the gyroscope (obtained at the optimal value of the coupling coefficient) is higher.

As can be seen from Fig. 2, propagation loss will reduce the peak value of the resonant curve of the resonator, and

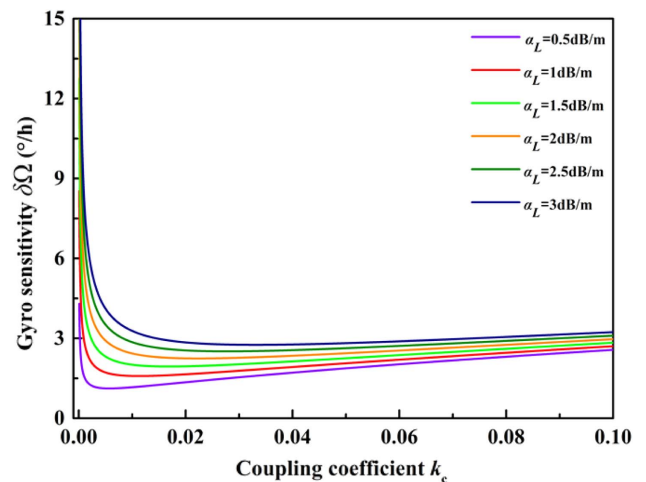


Fig. 1. Relationship between gyroscope sensitivity and coupling coefficient at different waveguide propagation losses.

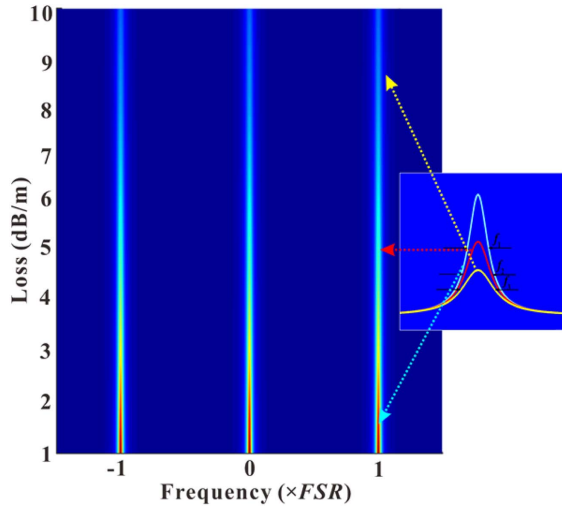


Fig. 2. Variation of the peak value of the resonance curve at different propagation losses.

the transmittance of the resonator will decrease. In addition, as the peak value of the resonant curve decreases, the full width at half-maximum (f) of the resonant curve also increases, as shown in the inset of Fig. 2. As $F = \text{FSR}/f$ (i.e., FSR is the free spectrum range), the F is reduced, thereby limiting the performance of the gyroscope. Thus, reducing the propagation loss of the waveguide resonator is the key to improving the performance of the gyroscope.

The single-polarization resonators can excite only one mode, thus suppressing the temperature-dependent polarization noise of the RIOG. Also, the polarization model of the resonator has been established in our previous work. Based on Eqs. (3)–(5) [19], we can see that the polarization extinction ratio of incident light is related to factors such as the polarization-to-axis angle at the input end of the waveguide, the polarization cross talk of the resonator coupler, and the polarization-dependent loss, all of which affect the resonator performance:

$$E_1 = \begin{bmatrix} \cos \sigma \\ e^{j\phi_0} \sin \sigma \end{bmatrix} E_x, \quad (3)$$

$$c_p = \begin{bmatrix} \cos \varepsilon & -\sin \varepsilon \\ \sin \varepsilon & \cos \varepsilon \end{bmatrix}, \quad (4)$$

$$B = \exp(j\beta L) \begin{bmatrix} \sqrt{1 - \alpha_x L} & 0 \\ 0 & \sqrt{1 - \alpha_y L} \end{bmatrix} \times \begin{bmatrix} \exp(j\frac{\Delta\beta}{2} L) & 0 \\ 0 & \exp(-j\frac{\Delta\beta}{2} L) \end{bmatrix}, \quad (5)$$

where E_1 is the electric field coupled into the waveguide resonator; σ is the angle corresponding to the polarization extinction ratio of the input light; ϕ_0 is the initial phase difference between TE and TM modes; E_x is the electric field strength of the light; c_p is the polarization cross-talk matrix of the coupler from the input waveguide to the resonator; ε is the equivalent cross-talk angle; B is the transfer matrix of the waveguide

resonator; α_x and α_y are the propagation losses for TE and TM modes; L is the perimeter of the resonator; and β and $\Delta\beta$ are the average and difference of the propagation constant, respectively.

When the polarization axis of the incident light deviates from the TE or TM mode directions of the waveguide, the primary and secondary polarization states of the resonator will be excited simultaneously. In addition, when the light passes through the coupler, polarization cross talk will occur in the TE and TM mode directions due to the influence of scattering of the medium, non-ideal waveguide geometry, internal stress, and other factors. Therefore, even if the input light is ideally

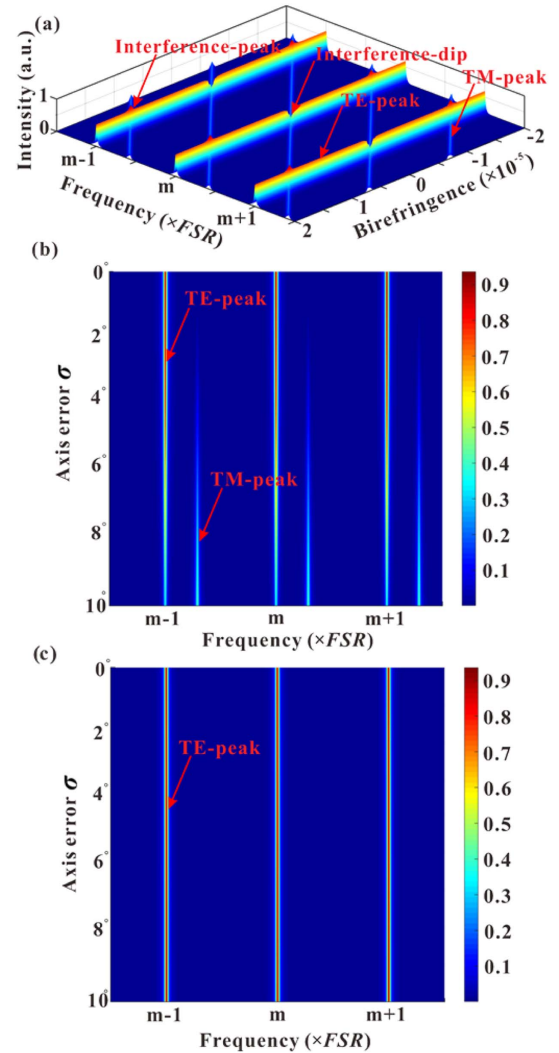


Fig. 3. (a) According to the polarization model [19] calculated three-dimensional resonance curve output at different birefringences; $D = 35$ mm, $\sigma = 30^\circ$, $\varepsilon = 3^\circ$, $\alpha_x = \alpha_y = 0.5$ dB/m, $k_x = k_y = 0.05$, $\alpha_{Cx} = \alpha_{Cy} = 0.01$ dB. (b) The relationship between the resonance curve of the resonator and the polarization axis error of the incident light; $D = 35$ mm, $\varepsilon = 0^\circ$, $\alpha_x = \alpha_y = 0.5$ dB/m, $k_x = k_y = 0.05$, $\alpha_{Cx} = \alpha_{Cy} = 0.01$ dB. (c) When the polarization-dependent loss $\alpha_y = 800$ dB/m, the relationship between the resonance curve of the resonator and the polarization axis error of the incident light; $D = 35$ mm, $\varepsilon = 10^\circ$, $\alpha_x = 0.5$ dB/m, $k_x = k_y = 0.05$, $\alpha_{Cx} = \alpha_{Cy} = 0.01$ dB.

linearly polarized and is strictly aligned with a certain polarization mode of the waveguide, due to the polarization cross talk of the actual coupler, there will still be light with the orthogonal polarization in the resonator. As long as the polarization cross talk is not zero, there will be alternating destructive and constructive interference, as shown in Fig. 3(a).

We assume that the waveguide coupler has no polarization cross talk if the polarization axis of the incident light has a certain angle with the TE mode direction, such that the energy distributions of the input light in the TE and the TM mode directions are different. The factors affecting the energy distribution of the incident light in the TE and the TM modes are equivalent to the polarization axis error. Obviously, the larger the polarization axis error, the larger the peak of the sub-polarization state, as shown in Fig. 3(b).

However, as Fig. 3(c) shows, if the resonator has sufficient polarization-dependent loss, then even in the presence of polarization axis error and coupler polarization cross talk, only one mode is excited inside the resonator. Therefore, having sufficient polarization-dependent loss is the key to realizing a single-polarization resonator.

3. Si₃N₄ RESONATOR STRUCTURE

In this paper, the structure of the Si₃N₄ waveguide resonator is shown in Fig. 4(a). The resonator is a 40 nm thick and 4 μm wide design. To improve the reciprocity of the gyroscope, the Si₃N₄ waveguide resonator we designed adopts a transmissive structure (i.e., add-drop configuration). The use of a curved waveguide at each entrance of the resonator enables the light source to be polarized before entering the Si₃N₄ waveguide resonator. The waveguide center spacing of the coupler is 12.5 μm, and the splitting ratio of the coupler was found to be 0.0063. Lower splitting ratios can allow the resonator to reach higher *F* [18]. However, at the same time, the transmittance of the resonator also decreases with decreasing splitting ratio. Therefore, a compromise in the splitting ratio must be made. Mode field distributions of TE and TM modes of Si₃N₄ waveguides are shown in Figs. 4(b) and 4(c), respectively. The effective refractive indices of TE and TM modes are obtained by simulation to be 1.4773 and 1.4456, respectively. To achieve the ideal polarizing performance, the waveguide adopts an ultralow-aspect-ratio structure so that the loss of TM mode can be improved as much as possible. The need for low leakage

loss imposes strict requirements on the cladding thickness of the Si₃N₄ waveguide, making it difficult to realize polarization by utilizing the longitudinal difference of the mode fields of the two polarization states. Since the effective refractive index of the TM mode is significantly lower than that of the TE mode, and, as can be seen from the mode field distribution, the waveguide's ability to confine the TM mode is relatively weak; when the bending radius decreases, the TM mode will not be fully confined in the waveguide at first, resulting in the generation of radiation modes that increase the bending loss of the TM mode.

The low-loss and single-polarization Si₃N₄ resonator must be fabricated in such a way to meet the requirements of high-precision gyroscopes:

$$\alpha_{\text{loss}} = \alpha_{\text{core}} + \alpha_{\text{top}} + \alpha_{\text{bottom}} + \alpha_{\text{sidewalls}} + \alpha_{\text{cladding}} \quad (6)$$

To further reduce propagation losses, we need to understand the characteristics of the film and determine which factors cause losses. As Eq. (6) shows, the three types of losses in the optical waveguide are surface scattering losses, absorption losses, and radiation losses. The scattering is the main source of propagation loss and is mainly caused by the surface roughness of the waveguide. Since the waveguide surface will never be completely smooth, the scattering loss will always exist. Absorption losses are mainly caused by the residual hydrogen during the deposition of the waveguide. In contrast, radiation losses are generally low, and occur when the bending radius is small.

As Figs. 4(b) and 4(c) show, for Si₃N₄ waveguides with ultralow aspect ratios, most of the light is transmitted in the silica cladding, and so this cladding must be of high quality. Specifically, it needs to be dense and have a low surface roughness, so the thermal oxidation process is the best choice. In addition, low-pressure chemical vapor deposition (LPCVD) with a high deposition temperature was used to deposit the Si₃N₄ core layer to ensure the uniformity and density of the surface while reducing the amount of hydrogen in the waveguide. While electron beam lithography was used to transfer the designed resonator pattern to the resist to prevent defects in the mask from being copied to the waveguide. Once the Si₃N₄ waveguide was fabricated, the waveguide chip could be cleaved for coupling and light testing.

Figure 5 shows the photograph with rear illumination inside the Si₃N₄ waveguide resonator taken with an infrared camera. By adjusting the focal length of the infrared camera and selecting an appropriate angle, the defects in the resonator due to the processing technology can be clearly observed. We can see that there are several obvious scattering points inside the Si₃N₄ waveguide resonator, which may be caused by residual impurities on the surface of the waveguide. As the upper cladding is bonded to the rest of the waveguide, the surface of the 1 μm silica grown by LPCVD must be polished before bonding. If the polishing is only partially successful, the surface of the silica remains rough, and there may even be residual particles on it, which would seriously affect the quality of bonding and form scattering points. As most of the light is transmitted in the cladding, any scattering on the cladding surface will become a major source of waveguide propagation loss. It will also cause backscattered noise, which will affect the performance of the RIOG. As the main obstacle to the successful application of

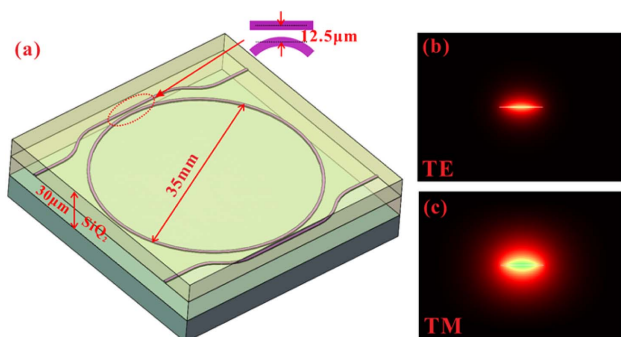


Fig. 4. (a) Structure diagram of the Si₃N₄ waveguide resonator, (b) TE mode, (c) TM mode.

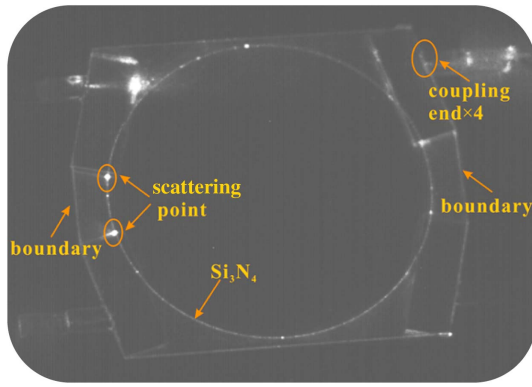


Fig. 5. Infrared photograph of the Si_3N_4 waveguide resonator with rear illumination showing scattered light.

RIOGs in engineering is the existence of high propagation loss caused by the processing defect, the processing technology must be further improved.

4. Si_3N_4 RESONATOR PERFORMANCE TEST

Figure 6 shows the relative test curve of the Si_3N_4 waveguide resonator. Figure 6(a) depicts the Si_3N_4 resonance curve test system. The output frequency of the tunable narrow linewidth laser is linearly changed by applying a triangular wave sweep signal. The light passes through a waveguide phase modulator (PM) to raise the polarization extinction ratio so as not to affect the test results before entering the resonator at point A. The output of the resonator was converted into a voltage signal by a photodiode (PD), and the relevant resonance curve is collected on the oscilloscope (OSC). Figure 6(b) shows the transmission resonance curve of the Si_3N_4 waveguide resonator. From the curve, it could be calculated that the FSR was 1.88 GHz, f was 12.53 MHz, F was 150, and Q was 1.54×10^7 (i.e., $Q = nLF/\lambda$, n is the refractive index of the

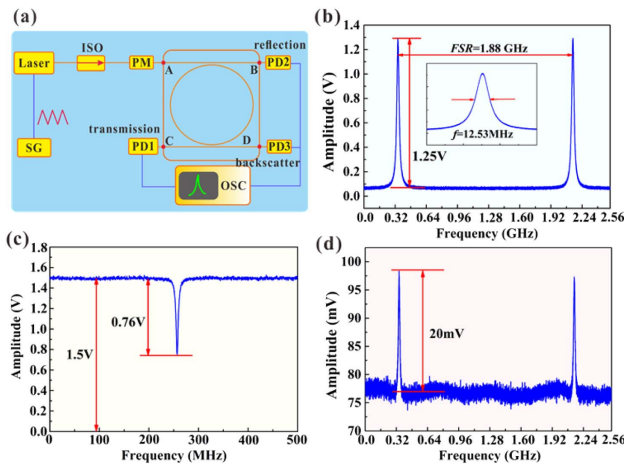


Fig. 6. Relative test curve of the Si_3N_4 waveguide resonator. SG, signal generator; ISO, isolator; PM, phase modulator; PD, photodetector; OSC, oscilloscope. (a) Resonance curve test system, (b) transmission curve, (c) reflection curve, and (d) backscattering curve.

waveguide, L is the length of the waveguide, λ is the wavelength of light). The resonance depth is 0.51 (i.e., $0.76/1.5$) from the resonance curve of the reflection end, as shown in Fig. 6(c). The propagation loss is 1.2 dB/m through calculation. As there were several scattering points in the resonator, it was also possible to study the backscattering characteristics of the Si_3N_4 waveguide resonator. As Fig. 6(d) shows, there is frequency-dependent backscattering, which could seriously affect the performance of the RIOG. However, mature carrier suppression technology can effectively suppress backscattered noise.

According to Eq. (3), in a waveguide resonator without polarization-dependent loss, when the polarization state of incident light is at a certain angle with the main polarization state of the resonator, the TE and TM polarization states will be excited simultaneously, and the relative position between the two resonant peaks will change with the change of waveguide birefringence. However, for the waveguide resonator with high polarization-dependent loss, the secondary polarization state in the incident light will be effectively suppressed. Therefore, the obtained sweep curve contains only one resonance peak, and the peak value will not fluctuate significantly with the change of waveguide birefringence.

To test this latter contention, we studied the polarization and temperature performance of the Si_3N_4 waveguide resonator. The test system was as in Fig. 6(a), except that before the light source enters the resonator, it is split with one part being rotated through 30° using fiber fusion splitting so that both polarization states of the light in the resonator can be excited. The primary and secondary polarization states can be distinguished by the magnitude of the resonance peak with 30° incidence.

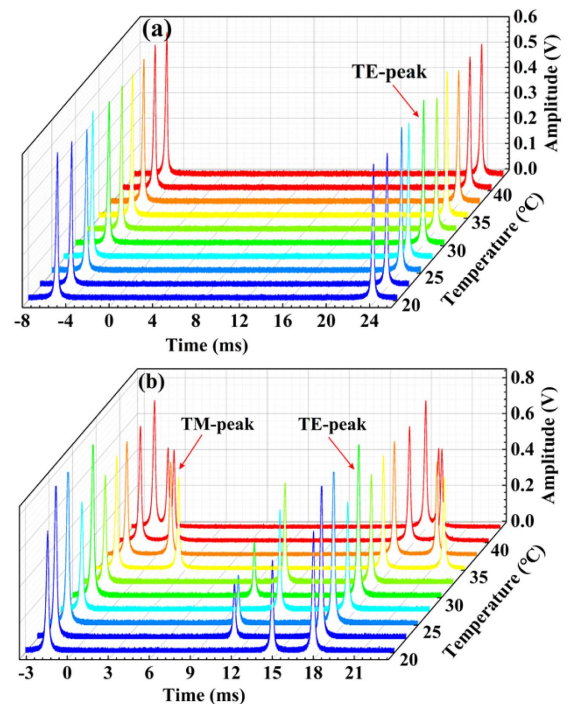


Fig. 7. Measured resonance curves at different temperatures: (a) Si_3N_4 waveguide resonator, (b) silica waveguide resonator.

Once again, the output light at the transmission end of the waveguide resonator was converted into a voltage signal by a PD which was displayed on an OSC. Finally, to measure the temperature performance of the Si_3N_4 waveguide resonator under the full birefringence period, the resonator was placed on an electric heating plate to accurately control the working temperature of the waveguide resonator. As Fig. 7(a) shows, only one resonant peak (i.e., TE peak) can be observed at all temperatures; the sharpness and shape of the main polarization resonant peak have not changed significantly with the change of temperature. This shows that the Si_3N_4 waveguide resonator has high polarization-dependent loss in a range of temperatures. This is beneficial to suppressing the polarization noise of the RIOG. As can be seen from Fig. 7(b), this is in contrast to the behavior of a silica waveguide resonator without polarization-dependent losses. Here, there are two resonance peaks (i.e., both TE and TM peaks) at different temperatures, with associated changes in the peak value of the resonance curve. As the TM peak represents polarization noise, this would limit the temperature stability of the RIOG that incorporates this silica-based waveguide.

5. EXPERIMENTAL RESULT OF RIOG

Figure 8 shows the RIOG measurement system based on a Si_3N_4 waveguide resonator with a bending radius of 17.5 mm. The light source, with a center wavelength and linewidth of 1550 nm and 1 kHz, respectively, enters the LiNbO_3 PM through the optical isolator, which prevents the reflected light from interfering with the laser and affecting the stability of the laser, and the half-wave voltage (V_π) of the LiNbO_3 is 5.385 V. The PM1 and PM2 of LiNbO_3 are modulated by sinusoidal signals, whose frequencies are 3.1 MHz and 2.3 MHz, respectively, and their amplitudes are 8.25 V. A low-frequency triangular wave signal with a frequency of 35.5 kHz and an amplitude of 10.77 V is applied to PM4 to provide additional carrier suppression to overcome the influence of backscattered noise, while PM3 with a sawtooth wave signal is used as a frequency shift driver to realize shift frequency and form the

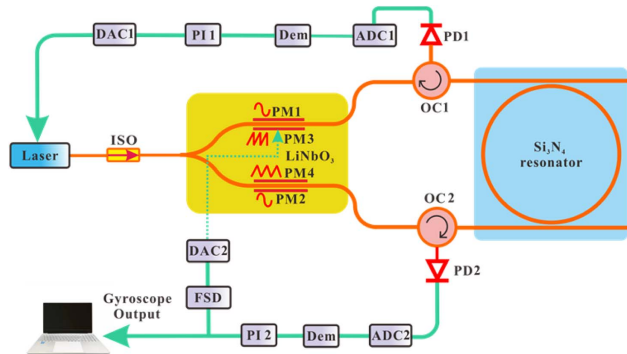


Fig. 8. RIOG measurement system based on the Si_3N_4 waveguide resonator. ISO, isolator; LiNbO_3 , lithium niobate; OC, optical circulator; PD, photodetector; ADC, analog digital converter; DAC, digital analog converter; Dem, demodulation; PI, proportional integral; FSD, frequency shift driver.

second closed loop. Also, the sawtooth wave amplitude is 10.77 V. The modulated light source is divided into two channels by the LiNbO_3 and enters the Si_3N_4 waveguide resonator from both ends. The RIOG uses a high reciprocity transmission system [26], and the transmission paths of the CW and CCW light are the same, which reduces the non-reciprocity error of the gyroscope. The light output by the Si_3N_4 waveguide resonator is converted to a voltage signal by the two photodiodes, PD1 and PD2. The signal of the CCW path output by PD1 is demodulated and used as a frequency locking signal for feedback control of the laser to adjust the laser output center frequency to keep it locked at the resonant frequency of the resonator. The CW signal output by PD2 is demodulated, and then fed back to the frequency shift driver through the proportional integral controller. When there is a rotation signal in the system, the frequency shift driver will generate a digital sawtooth signal, that is fed into PM3 to shift the frequency of the laser, so that the laser frequency in the CW direction of the resonator is also tracked and locked, creating the second closed loop. In this double-channel closed-loop detection scheme, the two channels are simultaneously locked at their resonant frequencies and the rotational angular velocity is obtained by reading the frequency difference directly.

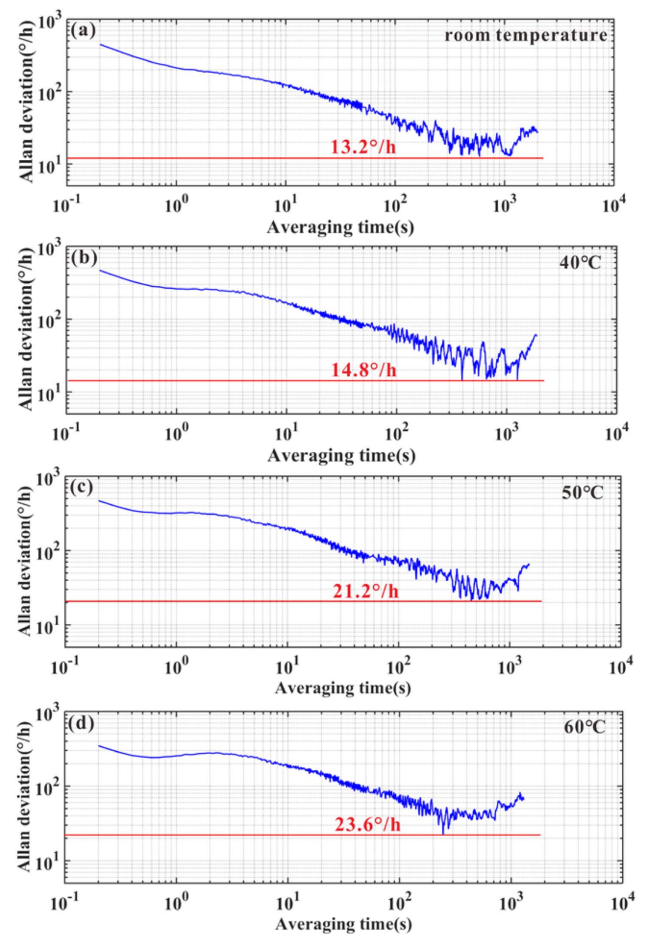


Fig. 9. Measurement results of the RIOG based on the Si_3N_4 waveguide resonator at rest from the Allan variance analysis result: (a) at room temperature, (b) at 40°C, (c) at 50°C, and (d) at 60°C.

When the Si_3N_4 waveguide resonator is placed in the room temperature environment ($\sim 26^\circ\text{C}$) and free from the temperature controller, a long-term bias stability (3600 s) of $13.2^\circ/\text{h}$ is successfully demonstrated from the Allan variance analysis result, as shown in Fig. 9(a). Experiments with the temperature of the system set to 40°C , 50°C , and 60°C returned long-term bias stability values of $14.8^\circ/\text{h}$, $21.2^\circ/\text{h}$, and $23.6^\circ/\text{h}$, respectively, as shown in Figs. 9(b)–9(d), which are at the same levels as the test results at room temperature. Thus, the RIOG shows excellent temperature stability, which indicates that the single-polarization Si_3N_4 waveguide resonator can effectively suppress the polarization noise. Meanwhile, the test results have high repeatability. As far as we know, this is the best result of the Si_3N_4 waveguide resonator-based RIOG reported so far, and it also promotes the engineering process of the RIOG.

6. CONCLUSION

In summary, a high-performance Si_3N_4 waveguide resonator with a bending radius of 17.5 mm, an F of 150, a Q of 1.54×10^7 , and a propagation loss of 1.2 dB/m was successfully fabricated. Experiments showed that the Si_3N_4 waveguide resonator has excellent single-polarization performance in a range of temperatures. The Si_3N_4 resonator was incorporated into an RIOG test system that showed long-term bias stability (3600 s) of $13.2^\circ/\text{h}$ at room temperature, $14.8^\circ/\text{h}$ at 40°C , $21.2^\circ/\text{h}$ at 50°C , and $23.6^\circ/\text{h}$ at 60°C . The experimental results had high repeatability and system stability. As far as we know, this is the best performance reported to date for the Si_3N_4 waveguide resonator-based RIOG. This advancement paves the way for the application of the RIOG.

Funding. National Natural Science Foundation of China (61973019).

Acknowledgment. The authors thank Lionix International (LXI) for their assistance in fabricating Si_3N_4 waveguides.

Disclosures. The authors declare no conflicts of interest.

Data Availability. Data underlying the results presented in this paper are not publicly available at this time but may be obtained from the authors upon reasonable request.

REFERENCES

1. T. Kessler, C. Hagemann, C. Grebing, T. Legero, U. Sterr, F. Riehle, M. J. Martin, L. Chen, and J. Ye, "A sub-40-mHz-linewidth laser based on a silicon single crystal optical cavity," *Nat. Photonics* **6**, 687–692 (2012).
2. S. Gundavarapu, G. M. Brodnik, M. Puckett, T. Huffman, D. Bose, R. Behunin, J. F. Wu, T. Q. Qiu, C. Pinho, N. Chauhan, J. Nohava, P. T. Rakich, K. D. Nelson, M. Salit, and D. J. Blumenthal, "Sub-hertz fundamental linewidth photonic integrated Brillouin laser," *Nat. Photonics* **13**, 60–67 (2019).
3. L. Stern, W. Zhang, D. Carlson, D. Popp, Z. Newman, S. Kang, J. Kitching, and S. Papp, "Ultrahigh-Q photonic-atomic laser," *Laser Photonics Rev.* **14**, 1900293 (2019).
4. P. Del'Haye, A. Schliesser, O. Arcizet, T. Wilkins, R. Holzwarth, and T. J. Kippenberg, "Optical frequency comb generation from a monolithic microresonator," *Nature* **450**, 1214–1217 (2007).
5. T. J. Kippenberg, A. L. Gaeta, M. Lipson, and M. L. Gorodetsky, "Dissipative Kerr solitons in optical microresonators," *Science* **361**, eaan8083 (2018).
6. D. R. Carlson, D. D. Hickstein, L. Alex, D. Stefan, W. Daron, N. Nima, C. Ian, N. R. Newbury, S. Kartik, and S. A. Diddams, "Self-referenced frequency combs using high-efficiency silicon-nitride waveguides," *Opt. Lett.* **42**, 2314–2317 (2017).
7. Y. H. Lai, M. G. Suh, Y. K. Lu, B. Shen, and K. Vahala, "Earth rotation measured by a chip-scale ring laser gyroscope," *Nat. Photonics* **14**, 345–349 (2020).
8. S. M. Lo, S. Hu, G. Gaur, Y. Kostoulas, and P. M. Fauchet, "Photonic crystal microring resonator for label-free biosensing," *Opt. Express* **25**, 7046–7054 (2017).
9. Z. Tu, D. Gao, M. Zhang, and D. Zhang, "High-sensitivity complex refractive index sensing based on Fano resonance in the subwavelength grating waveguide micro-ring resonator," *Opt. Express* **25**, 20911–20922 (2017).
10. P. P. Khial, A. D. White, and A. Hajimiri, "Nanophotonic optical gyroscope with reciprocal sensitivity enhancement," *Nat. Photonics* **12**, 671–675 (2018).
11. J. T. Geng, L. Yang, S. H. Zhao, and Y. G. Zhang, "Resonant micro-optical gyro based on self-injection locking," *Opt. Express* **28**, 32907–32915 (2020).
12. G. Sagnac, "On the proof of the reality of the luminiferous aether by the experiment with a rotating interferometer," *Comptes Rendus* **157**, 1410–1413 (1913).
13. G. A. Sanders, M. G. Prentiss, and S. Ezekiel, "Passive ring resonator method for sensitive inertial rotation measurements in geophysics and relativity," *Opt. Lett.* **6**, 569–571 (1981).
14. A. Li and W. Bogaerts, "Using backscattering and backcoupling in silicon ring resonators as a new degree of design freedom," *Laser Photonics Rev.* **13**, 1800244 (2019).
15. A. Li, V. V. Thomas, D. H. Peter, B. Peter, and B. Wim, "Backscattering in silicon microring resonators: a quantitative analysis," *Laser Photonics Rev.* **10**, 420–431 (2016).
16. J. J. Wang, L. S. Feng, Q. W. Wang, H. C. Jiao, and X. Wang, "Suppression of backreflection error in resonator integrated optic gyro by the phase difference traversal method," *Opt. Lett.* **41**, 1586–1589 (2016).
17. L. S. Feng, M. Lei, H. L. Liu, Y. Z. Zhou, and J. J. Wang, "Suppression of back-reflection noise in a resonator integrated optic gyro by hybrid phase-modulation technology," *Appl. Opt.* **52**, 1668–1675 (2013).
18. C. K. Feng, D. K. Zhang, Y. G. Zhang, C. Qing, H. H. Ma, H. Li, and L. S. Feng, "Resonant integrated optical gyroscope based on Si_3N_4 waveguide ring resonator," *Opt. Express* **29**, 43875–43884 (2021).
19. C. K. Feng, D. N. Liu, H. H. Ma, C. Qing, H. Li, and L. S. Feng, "Design, fabrication and test of transmissive Si_3N_4 waveguide ring resonator," *IEEE Sens. J.* **21**, 22918–22926 (2021).
20. J. R. Haavisto, "Thin film waveguides for inertial sensors," *Proc. SPIE* **412**, 221–228 (1983).
21. A. Morand, C. Sanchez-Perez, P. Benech, S. Tedjini, and D. Bose, "Integrated optical waveguide polarizer on glass with a birefringent polymer overlay," *IEEE Photonics Technol. Lett.* **10**, 1599–1601 (1998).
22. H. Lee, T. Chen, J. Li, K. Y. Yang, S. Jeon, O. Painter, and K. J. Vahala, "Chemically etched ultrahigh-Q wedge-resonator on a silicon chip," *Nat. Photonics* **6**, 369–373 (2012).
23. B. Stern, X. C. Ji, A. Dutt, and M. Lipson, "Compact narrow-linewidth integrated laser based on a low-loss silicon nitride ring resonator," *Opt. Lett.* **42**, 4541–4544 (2017).
24. E. H. Dirani, L. Youssef, C. Petit-Etienne, K. Sebastien, G. Philippe, M. Christelle, P. Erwine, and S. Corrado, "Ultralow-loss tightly confining Si_3N_4 waveguides and high-Q microresonators," *Opt. Express* **27**, 30726–30740 (2019).
25. H. L. Ma, W. Y. Wang, Y. Ren, and Z. H. Jin, "Low-noise low-delay digital signal processor for resonant micro optic gyro," *IEEE Photonics Technol. Lett.* **25**, 198–201 (2013).
26. Q. Wang, L. S. Feng, H. Li, X. Wang, Y. Z. Jia, and D. N. Liu, "Enhanced differential detection technique for the resonator integrated optic gyro," *Opt. Lett.* **43**, 2941–2944 (2018).

27. X. C. Ji, S. Roberts, M. Corato-Zanarella, and M. Lipson, "Methods to achieve ultra-high quality factor silicon nitride resonators," *APL Photonics* **6**, 071101 (2021).
28. A. Mohanty, Q. Li, M. A. Tadayon, S. P. Roberts, G. R. Bhatt, E. Shim, X. C. Ji, J. Cardenas, S. A. Miller, A. Kepecs, and M. Lipson, "Reconfigurable nanophotonic silicon probes for sub-millisecond deep-brain optical stimulation," *Nat. Biomed. Eng.* **4**, 223–231 (2020).
29. X. C. Ji, X. W. Yao, Y. Gan, A. Mohanty, M. A. Tadayon, C. P. Hendon, and M. Lipson, "On-chip tunable photonic delay line," *APL Photonics* **4**, 090803 (2019).
30. X. Ji, F. A. S. Barbosa, S. P. Roberts, A. Dutt, J. Cardenas, Y. Okawachi, A. Bryant, A. L. Gaeta, and M. Lipson, "Ultra-low-loss on-chip resonators with sub-milliwatt parametric oscillation threshold," *Optica* **4**, 619–624 (2017).
31. M. H. P. Pfeiffer, J. Q. Liu, A. S. Raja, T. Morais, B. Ghadiani, and T. J. Kippenberg, "Ultra-smooth silicon nitride waveguides based on the damascene reflow process: fabrication and loss origins," *Optica* **5**, 884–892 (2018).
32. M. Sinclair, K. Gallacher, M. Sorel, J. C. Bayley, E. McBrearty, R. W. Millar, S. Hild, and D. J. Paul, "1.4 million Q factor Si_3N_4 micro-ring resonator at 780 nm wavelength for chip-scale atomic systems," *Opt. Express* **28**, 4010–4020 (2020).
33. K. Wu and A. W. Poon, "Stress-released Si_3N_4 fabrication process for dispersion-engineered integrated silicon photonics," *Opt. Express* **28**, 17708–17722 (2020).
34. J. F. Bauters, M. J. R. Heck, D. D. John, J. S. Barton, C. M. Bruinink, A. Leinse, R. G. Heideman, D. J. Blumenthal, and J. E. Bowers, "Planar waveguides with less than 0.1 dB/m propagation loss fabricated with wafer bonding," *Opt. Express* **19**, 24090–24101 (2011).
35. D. T. Spencer, J. F. Bauters, M. J. R. Heck, and J. E. Bowers, "Integrated waveguide coupled Si_3N_4 resonators in the ultrahigh-Q regime," *Optica* **1**, 153–157 (2014).
36. M. W. Puckett, K. K. Liu, N. Chauhan, Q. C. Zhao, N. J. Jin, H. T. Cheng, J. F. Wu, R. O. Behunin, P. T. Rakich, K. D. Nelson, and D. J. Blumenthal, "422 million intrinsic quality factor planar integrated all-waveguide resonator with sub-MHz linewidth," *Nat. Commun.* **12**, 934 (2021).
37. L. S. Feng, J. J. Wang, Y. Z. Zhi, Y. C. Tang, Q. W. Wang, H. C. Li, and W. Wang, "Transmissive resonator optic gyro based on silica waveguide ring resonator," *Opt. Express* **22**, 27565–27575 (2014).